Eur. Phys. J. A **22**, 37–45 (2004)
DOI 10.1140/epja/i2003-10227-7

THE EUROPEAN PHYSICAL JOURNAL A

Relativistic Hartree-Bogoliubov description of deformed light nuclei

G.A. Lalazissis[1,2], D. Vretenar[2,3], and P. Ring[2,a]

[1] Department of Theoretical Physics, Aristotle University of Thessaloniki, Thessaloniki GR-54124, Greece
[2] Physik-Department der Technischen Universität München, D-85748 Garching, Germany
[3] Physics Department, Faculty of Science, University of Zagreb, 10 000 Zagreb, Croatia

Received: 27 August 2003 / Revised version: 12 March 2004 /
Published online: 19 October 2004 –
Communicated by G. Orlandini

Abstract. The Relativistic Hartree-Bogoliubov model is applied in the analysis of ground-state properties of Be, B, C, N, F, Ne and Na isotopes. The model uses the NL3 effective interaction in the mean-field Lagrangian, and describes pairing correlations by the pairing part of the finite-range Gogny interaction D1S. Neutron separation energies, quadrupole deformations, nuclear matter radii, and differences in radii of proton and neutron distributions are compared with recent experimental data.

PACS. 21.60.Jz Hartree-Fock and random-phase approximations – 21.10.Gv Mass and neutron distributions – 27.20.+n $6 \leq A \leq 19$ – 27.30.+t $20 \leq A \leq 38$

1 Introduction and outline of the model

During the last decade a large quantity of data on light nuclei with $4 \leq Z \leq 12$ has become available. In particular, measurements of interaction cross-sections by using radioactive nuclear beams at intermediate and relativistic energies, have provided important data on nuclear radii [1–9]. The nuclear radius is a fundamental quantity which, in principle, provides information on the effective nuclear potential, shell effects and ground-state deformation. For exotic nuclei with extreme values of the neutron-to-proton ratio, particularly important is the isospin dependence of nuclear radii which can signal the onset of new phenomena like, for example, the formation of skin and halo structures. Data on ground-state deformations are also very important for the study of shell effects in exotic nuclei. In particular, they reflect major modifications in the shell structures, the disappearance of standard and the occurrence of new magic numbers. Different ground-state deformations of proton and neutron density distributions are expected in some nuclei with extreme isospin projection quantum number T_z. Another source of information on the effective nuclear potential in exotic systems at the limits of stability are the single-nucleon separation energies. The neutron drip line has been reached for nuclei up to $Z = 9$ [10]. On the proton-rich side the drip line has been experimentally fully mapped up to $Z = 21$, and possibly for odd-Z nuclei up to In [11,12]. In very neutron-rich nuclei the weak binding of the outermost neutrons causes the formation of the neutron skin on the surface of a nucleus, and the formation of one- and two-neutron halo structures. The established two-neutron halo nuclei are ^{6}He, ^{11}Li, and ^{14}Be, and the one-neutron halo nuclei are ^{11}Be and ^{19}C. Recent data [8,9] present evidence for a one-neutron halo in ^{22}N, ^{23}O and ^{24}F. The formation of the neutron skin is well established in the neutron-rich Na isotopes [3,5], and the related phenomenon of low-lying pygmy isovector dipole resonances has recently been observed in O isotopes [13]. On the proton-rich side evidence has been reported for the existence of a proton skin in ^{20}Mg [14], and a beautiful example of exotic decay modes is provided by the two-proton emitter ^{18}Ne [15].

In the present work the Relativistic Hartree-Bogoliubov (RHB) model is applied in the analysis of ground-state properties of Be, B, C, N, F, Ne and Na isotopes. Based on the relativistic mean-field theory and on the Hartree-Fock-Bogoliubov framework, the RHB model provides a unified description of mean-field and pairing correlations. It has been successfully applied in the description of nuclear-structure phenomena in exotic nuclei far from the valley of β-stability and of the physics of the drip lines. On the neutron-rich side RHB studies include: the halo phenomenon in light nuclei [16,17], properties of light nuclei near the neutron drip [18], the reduction of the spin-orbit potential in nuclei with extreme isospin values [19], the deformation and shape coexistence phenomena that result from the suppression of the spherical $N = 28$ shell gap in neutron-rich nuclei [20], properties of

[a] e-mail: Ring@Physik.TU-Muenchen.de

neutron-rich Zr nuclei [21,22], Ni and Sn isotopes [23–25]. In proton-rich nuclei the RHB model has been used to map the drip line from $Z = 31$ to $Z = 73$, and the phenomenon of ground-state proton radioactivity has been studied [26–28]. In a study of the isovector channel of the RHB model [29], a very good agreement with experimental data has been obtained for ground-state properties of nuclei that belong to the $A = 20$ isobaric sequence.

In the framework of the Relativistic Mean-Field (RMF) approximation [30] nucleons are described as point particles that move independently in the mean fields which originate from the nucleon-nucleon interaction. The theory is fully Lorentz invariant. Conditions of causality and Lorentz invariance impose that the interaction is mediated by the exchange of point-like effective mesons, which couple to the nucleons at local vertices: the isoscalar scalar σ-meson, the isoscalar vector ω-meson and the isovector vector ρ-meson. The model is based on the one-boson exchange description of the nucleon-nucleon interaction. We start from the effective Lagrangian density

$$\begin{aligned}\mathcal{L} = & \bar{\psi}\left(i\gamma\cdot\partial - m\right)\psi \\ & + \frac{1}{2}(\partial\sigma)^2 - U(\sigma) - \frac{1}{4}\Omega_{\mu\nu}\Omega^{\mu\nu} + \frac{1}{2}m_\omega^2\omega^2 \\ & - \frac{1}{4}\vec{R}_{\mu\nu}\vec{R}^{\mu\nu} + \frac{1}{2}m_\rho^2\vec{\rho}^{\,2} - \frac{1}{4}F_{\mu\nu}F^{\mu\nu} \\ & - g_\sigma\bar{\psi}\sigma\psi - g_\omega\bar{\psi}\gamma\cdot\omega\psi - g_\rho\bar{\psi}\gamma\cdot\vec{\rho}\,\vec{\tau}\psi \\ & - e\bar{\psi}\gamma\cdot A\frac{(1-\tau_3)}{2}\psi\ . \end{aligned} \tag{1}$$

Vectors in isospin space are denoted by arrows, and boldfaced symbols will indicate vectors in ordinary three-dimensional space. The Dirac spinor ψ denotes the nucleon with mass m. m_σ, m_ω, and m_ρ are the masses of the σ-meson, the ω-meson, and the ρ-meson, respectively. g_σ, g_ω, and g_ρ are the corresponding coupling constants for the mesons to the nucleon. $e^2/4\pi = 1/137.036$. The coupling constants and unknown meson masses are parameters, adjusted to fit data of nuclear matter and of finite nuclei. $U(\sigma)$ denotes the non-linear σ self-interaction [31]

$$U(\sigma) \ = \ \frac{1}{2}m_\sigma^2\sigma^2 + \frac{1}{3}g_2\sigma^3 + \frac{1}{4}g_3\sigma^4, \tag{2}$$

and $\Omega^{\mu\nu}$, $\vec{R}^{\mu\nu}$, and $F^{\mu\nu}$ are field tensors:

$$\Omega^{\mu\nu} = \partial^\mu\omega^\nu - \partial^\nu\omega^\mu, \tag{3}$$

$$\vec{R}^{\mu\nu} = \partial^\mu\vec{\rho}^{\,\nu} - \partial^\nu\vec{\rho}^{\,\mu}, \tag{4}$$

$$F^{\mu\nu} = \partial^\mu A^\nu - \partial^\nu A^\mu. \tag{5}$$

The lowest order of the quantum field theory is the *mean-field* approximation: the meson field operators are replaced by their expectation values. The A nucleons, described by a Slater determinant $|\Phi\rangle$ of single-particle spinors ψ_i, $(i = 1, 2, \ldots, A)$, move independently in the classical meson fields. The sources of the meson fields are defined by the nucleon densities and currents. The ground state of a nucleus is described by the stationary self-consistent solution of the coupled system of Dirac and Klein-Gordon equations. In the static case for an even-even system, time-reversal invariance forbids currents in the nucleus, and therefore the spatial vector components $\boldsymbol{\omega}, \boldsymbol{\rho}_3$ and $\mathbf{A}$ of the vector meson fields vanish. The Dirac equation reads

$$\begin{aligned}\Big\{ & -i\boldsymbol{\alpha}\cdot\boldsymbol{\nabla} + \beta(m + g_\sigma\sigma) + g_\omega\omega^0 \\ & + g_\rho\tau_3\rho_3^0 + e\frac{(1-\tau_3)}{2}A^0\Big\}\psi_i = \varepsilon_i\psi_i \end{aligned} \tag{6}$$

In addition to the self-consistent mean-field potential, pairing correlations have to be included in order to describe ground-state properties of open-shell nuclei. In the framework of the relativistic Hartree-Bogoliubov model, the ground state of a nucleus $|\Phi\rangle$ is represented by the product of independent single-quasiparticle states. These states are eigenvectors of a generalized single-nucleon Hamiltonian that contains two average potentials: the self-consistent mean-field $\hat{\Gamma}$ which encloses all the long-range particle-hole (ph) correlations, and a pairing field $\hat{\Delta}$ which sums up the particle-particle (pp) correlations. In the Hartree approximation for the self-consistent mean field, the relativistic Hartree-Bogoliubov equations read

$$\begin{pmatrix} \hat{h}_{\rm D} - m - \lambda & \hat{\Delta} \\ -\hat{\Delta}^* & -\hat{h}_{\rm D} + m + \lambda \end{pmatrix} \begin{pmatrix} U_k(\mathbf{r}) \\ V_k(\mathbf{r}) \end{pmatrix} = E_k \begin{pmatrix} U_k(\mathbf{r}) \\ V_k(\mathbf{r}) \end{pmatrix}. \tag{7}$$

where $\hat{h}_{\rm D}$ is the single-nucleon Dirac Hamiltonian (6), and m is the nucleon mass. The chemical potential λ has to be determined by the particle number subsidiary condition in order that the expectation value of the particle number operator in the ground state equals the number of nucleons. $\hat{\Delta}$ is the pairing field. The column vectors denote the quasiparticle spinors and E_k are the quasiparticle energies.

The self-consistent solution of the Dirac-Hartree-Bogoliubov integro-differential eigenvalue equations and Klein-Gordon equations for the meson fields determines the nuclear ground state. For systems with spherical symmetry, *i.e.* single closed-shell nuclei, the coupled system of equations has been solved using finite element methods in coordinate space [17,32], using the shooting method with Runge-Kutta alghoritms in coordinate space [24,25], and by expansion in a basis of a spherical harmonic oscillator [23]. For deformed nuclei the present version of the model does not include solutions in coordinate space. The Dirac-Hartree-Bogoliubov equations and the equations for the meson fields are solved by expanding the nucleon spinors $U_k(\mathbf{r})$ and $V_k(\mathbf{r})$, and the meson fields, in terms of the eigenfunctions of a deformed axially symmetric oscillator potential [33]. For nuclei at the drip lines, however, solutions in configurational representation might not provide an accurate description of properties that crucially depend on the spatial extension of nucleon densities, as for example nuclear radii. In less exotic nuclei on the neutron-rich side, or for proton-rich nuclei, an expansion in a large oscillator basis should provide sufficiently accurate solutions. In particular, proton-rich nuclei are stabilized by the Coulomb barrier which tends to localize the proton

density in the nuclear interior and thus prevents the formation of objects with extreme spatial extension. The calculations for the present analysis have been performed by an expansion in 12 oscillator shells for the fermion fields, and 20 shells for the boson fields. A simple blocking procedure is used in the calculation of odd-proton and/or odd-neutron systems. The blocking calculations are performed without breaking the time-reversal symmetry. A detailed description of the Relativistic Hartree-Bogoliubov model for deformed nuclei can be found in ref. [27].

Taking into account that the quasiparticle wave functions in the Hartree-Bogoliubov equations (7) contain large and small components, the pairing field $\hat{\Delta}$ can be written in the form

$$\begin{pmatrix} \hat{\Delta}_{++} & \hat{\Delta}_{+-} \\ \hat{\Delta}_{-+} & \hat{\Delta}_{--} \end{pmatrix}. \tag{8}$$

By using relativistic potentials with cut-off parameters, recent calculations of finite nuclei [34] have shown that the matrix elements of the terms $\hat{\Delta}_{-+}$ and $\hat{\Delta}_{+-}$, which couple large and small components, are orders of magnitude smaller than the matrix elements of the corresponding off-diagonal term $\boldsymbol{\sigma}\boldsymbol{\nabla}$ of the Dirac Hamiltonian $h_{\rm D}$. Pairing properties are determined by correlations in an energy window of a few MeV around the Fermi surface, and therefore also $\hat{\Delta}_{--}$ has no effect on pairing in finite nuclei. Thus, a good approximation is to neglect the fields $\hat{\Delta}_{-+}$, $\hat{\Delta}_{+-}$ and $\hat{\Delta}_{--}$ in the RHB equations, and to use a non-relativistic potential in the calculation of the field $\hat{\Delta}_{++}$.

2 Ground-state properties of deformed light nuclei

In parallel with the experimental work of the last decade, many theoretical analyses of the structure of nuclei in the mass region $10 \leq A \leq 30$ have been performed. Both microscopic mean-field and shell-model approaches, as well as various microscopic cluster models, have been used to study properties of ground and excited states of isotopic and isobaric sequences, and to describe specific structure phenomena in exotic nuclei. It has been shown that theoretical models reproduce the global trends of nuclear sizes and binding energies. However, special assumptions have to be made, or even new models have to be designed, in order to describe more exotic phenomena like, for example, the location of the neutron drip line in oxygen, or the ground-state deformation of ^{32}Mg.

In ref. [18] we reported spherical RHB calculations of neutron-rich isotopes of N, O, F, Ne, Na and Mg. By using several standard RMF effective interactions, we analyzed the location of the neutron drip line, the reduction of the spin-orbit interaction, r.m.s. radii, changes in surface properties, and the formation of neutron skins and of neutron halos. It was shown that, even without taking into account the deformation of the mean field, the RHB model correctly describes the global trends of the observed ground-state properties. The exception is, of course, the location of the neutron drip line in oxygen, which none of the RMF effective interactions reproduces.

In the study of ref. [29] we performed deformed RHB calculations of ground-state properties of nuclei that belong to the $A = 20$ isobaric sequence. The NL3 effective interaction [35] was used for the mean-field Lagrangian, and pairing correlations were described by the pairing part of the finite-range Gogny interaction D1S [36]. This particular combination of effective forces in the *ph* and *pp* channels has been used in most of our recent applications of the RHB theory. RHB results for binding energies, neutron and proton ground-state density distributions, quadrupole deformations, nuclear matter radii, and proton radii were compared with available experimental data. The very good agreement with the observed ground-state properties as a function of the isospin projection T_z, led to the conclusion that the isovector channel of the NL3 interaction is correctly parameterized and that this effective force can be used to describe not only medium-heavy and heavy nuclei [23,26–28], but also properties of relatively light nuclei far from β-stability. Other effective RMF interactions that have been successfully employed in the description of ground-state properties of spherical and deformed nuclei, include the parameter sets NL1 [37], NL-SH [38], and TM1 [39].

In the present work we apply the RHB model, with the NL3 + D1S effective interaction, in the analysis of ground-state properties of Be, B, C, N, F, Ne and Na isotopic sequences. We perform deformed RHB calculations and compare radii, separation energies and quadrupole deformations with available experimental data and with the predictions of the Finite-Range Droplet Model (FRDM) [40]. Of course, when the RHB equations are solved in the configuration space of harmonic-oscillator basis states, for nuclei at the drip lines one does not expect an accurate description of properties that crucially depend on the spatial extension of the wave functions of the outermost nucleons, especially on the neutron-rich side. Thus, we do not attempt to describe radii of halo nuclei. We also do not repeat the spherical calculations of O isotopes, which can be found in ref. [18].

In fig. 1 we display the proton, neutron and matter radii, ground-state quadrupole deformations, and one-neutron separation energies of beryllium isotopes, calculated with the NL3 + Gogny D1S effective interaction. The RHB values are compared with the experimental radii [1,6,8] and separation energies [41]. The calculated matter radii reproduce the trend of the experimental values, except for the halo nucleus ^{11}Be [42,43]. For the proton radii, on the other hand, the theoretical values are considerably lower than the experimental ones [1], especially for ^{14}Be, though it should be noted that the experimental proton radius has a very large uncertainty. The calculated neutron skin in ^{14}Be is very large: $r_n - r_p = 0.71$ fm, and also the deformations of the proton and neutron densities in this nucleus are very different. ^{14}Be has a large prolate deformation $\beta_2 = 0.36$ and the ratio of neutron to proton quadrupole moments is $Q_n/Q_p = 3.6$. The one-neutron

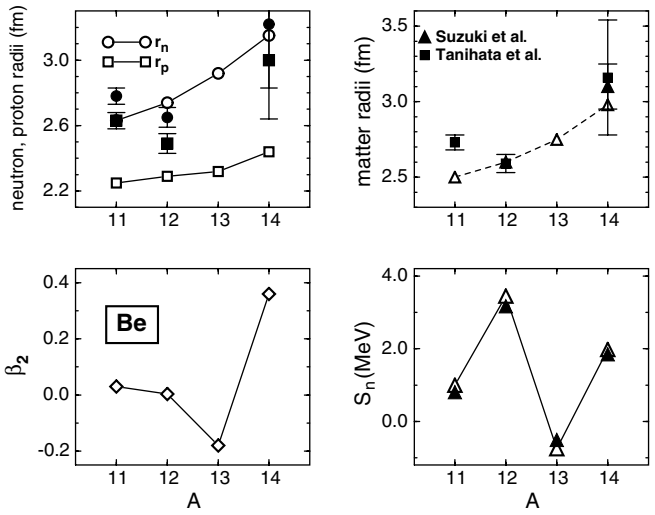

Fig. 1. Proton, neutron and matter radii, ground-state quadrupole deformations and one-neutron separation energies of beryllium isotopes, calculated with the NL3 + Gogny D1S effective interaction. The theoretical values are compared with the experimental radii [1,6,8] and separation energies [41].

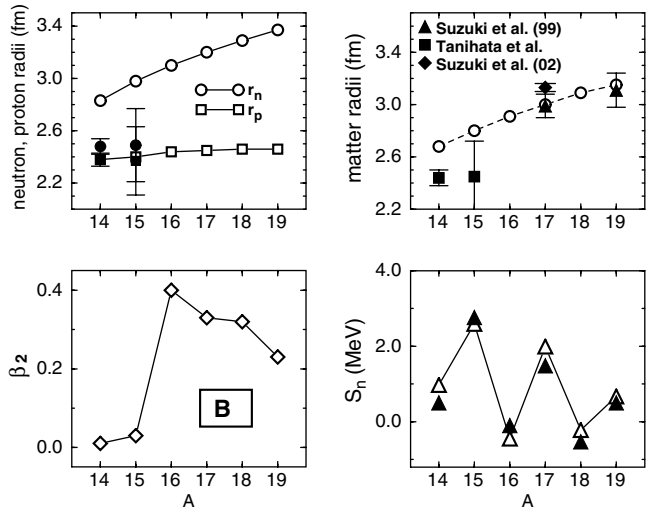

Fig. 2. Same as in fig. 1, but for boron isotopes. The experimental radius (diamond) is from ref. [7].

separation energies are also in excellent agreement with the empirical values [41]. In particular, ^{13}Be is predicted to be unbound by 180 keV.

In fig. 2 the same comparison is shown for neutron-rich boron isotopes. The calculated matter radii are in excellent agreement with the recent experimental data [6,7] for ^{17}B and ^{19}B, while they are larger than the older experimental values [1] for ^{14}B and ^{15}B. Unlike in the case of Be, the calculated proton radii for these two nuclei agree well with the empirical values, but the theoretical neutron radii are much larger. The RHB calculation also predicts ^{14}B and ^{15}B to be spherical in the ground state, while the heavier boron isotopes are strongly prolate deformed. We find a sudden onset of strong deformation at $A = 16$. The experimentally observed Q-moments change rather

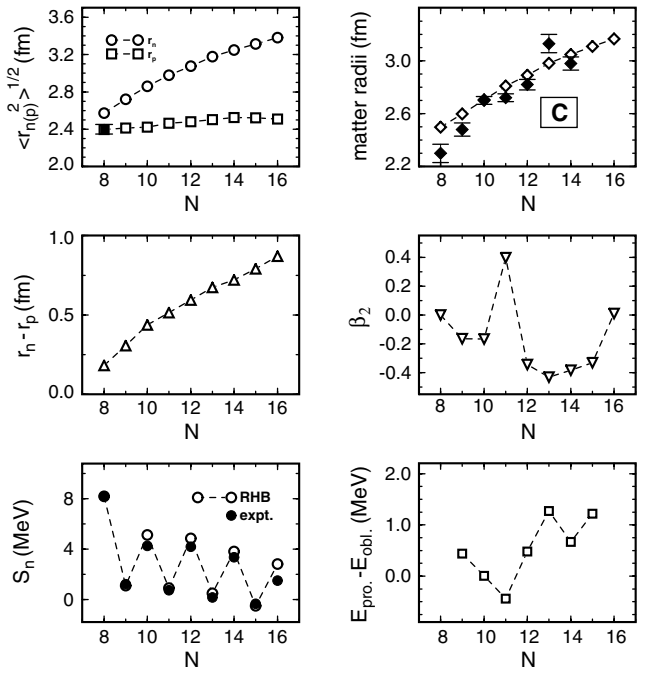

Fig. 3. Proton, neutron and matter radii, skin thicknesses, ground-state quadrupole deformations, one-neutron separation energies and energy differences between prolate and oblate minima for carbon isotopes. The theoretical values are compared with the experimental radii [44,8] and separation energies [41].

smoothly from $|Q(^{13}\mathrm{B})| = 36.9$ mb over $|Q(^{15}\mathrm{B})| = 38.0$ mb to $|Q(^{17}\mathrm{B})| = 38.8$ mb. This can be explained as a deficiency of the mean-field theory, which shows always very sharp phase transitions reflecting the properties of infinite systems where fluctuations can be neglected. In such light nuclei fluctuations play an important role and therefore the experimental quadrupole moments change usually much more smoothly than those predicted by mean-field calculations. The separation energies agree with the empirical values [41], and we note that both ^{16}B and ^{18}B are predicted to be neutron unbound.

The calculated quantities which characterize the ground states of neutron-rich carbon isotopes are displayed in fig. 3. The proton radius of ^{14}C is compared with the experimental value from ref. [44], and the matter radii are shown in comparison with very recent experimental data [8]. The trend of the experimental matter radii is clearly reproduced by the RHB calculation. Of course, for the one-neutron halo nucleus ^{19}C [45] the calculation in the harmonic-oscillator configuration space cannot reproduce the anomalous matter radius. The RHB model predictions for the one-neutron separation energies are in agreement with the empirical values [41], though the theoretical values are slightly larger for the even-N isotopes. In particular, from an analysis of the angular distribution of the $^{18}\mathrm{C} + n$ center of mass [46], the neutron separation energy is determined to be 530 ± 130 keV, and the RHB calculated value is 510 keV. ^{14}C and ^{22}C are spherical, and all other neutron-rich carbon isotopes, except ^{17}C,

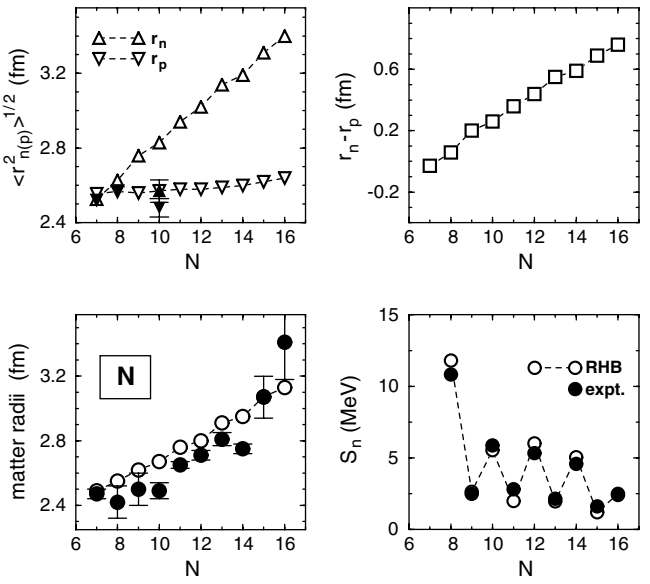

Fig. 4. The RHB theoretical proton, neutron and matter radii, skin thicknesses, and one-neutron separation energies of nitrogen isotopes, compared with the experimental radii [44,2,8] and separation energies [41].

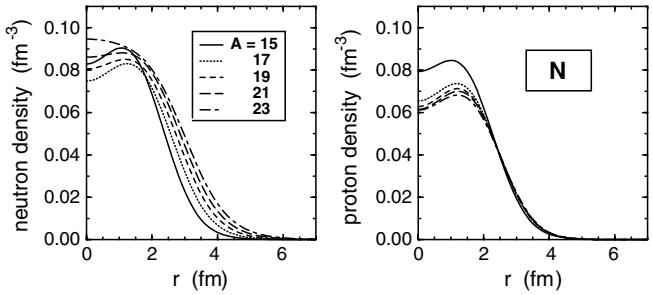

Fig. 5. Self-consistent RHB neutron and proton density profiles of nitrogen isotopes.

have oblate ground states. We have to keep in mind, however, that there are always two minima, one with prolate and one with oblate deformation, which are often very close in energy. In fig. 3 we therefore also plot the energy differences between these two minima. In ^{15}C and in ^{16}C we find very small differences of only a few hundred keV. It depends on fine details of the single-particle spectrum, which of these two minima is lower. It turns out that the mean-field theory is not always accurate enough to describe such details properly and therefore it can happen that the sign of the deformation is not properly reproduced in the calculation. This is a general property of mean-field calculations. One example is the nucleus ^{15}C, which is found to be oblate in our calculations. This means that we put the last neutron in the $K = 5/2$ orbit. Experimentally the ground state of this isotope has spin 1/2, *i.e.* one expects in this case a prolate deformation, *i.e.* the sign of the deformation is not properly reproduced in this case.

The RHB results for nitrogen isotopes are shown in fig. 4. The proton radii are compared with the experimental values from ref. [44]. The calculated matter radii reproduce the global trend of the experimental data [8], but not the sudden increase of the radii at $N = 15$. In the recent measurement of the interaction cross-sections for $^{14-23}$N, $^{16-24}$O, and $^{18-26}$F on carbon targets at relativistic energies [8], a sharp increase of matter radii at $N = 15$ was observed in all three isotopic chains (see also fig. 6). The deduced matter radii for ^{22}N, ^{23}O, and ^{24}F are much larger than those of their respective neighbors with one neutron less, and the deduced nucleon density distributions show a long neutron tail for these nuclei, comparable to that in ^{11}Be. It was therefore concluded that these three nuclei exhibit a one-neutron halo structure. Since they are spherical, the halo structure should result from the odd neutron occupying the $2s_{1/2}$ orbital. The absence of the centrifugal barrier for an s-orbital facilitates the formation of the long tail of the wave function, *i.e.* the halo structure. However, in ref. [8] it was also noted that the one-neutron separation energies for ^{22}N, ^{23}O, and ^{24}F are larger than 1 MeV (1.22 ± 0.22 MeV, 2.74 ± 0.12 MeV and 3.86 ± 0.11 MeV, respectively), and much larger than in ^{11}Be and ^{19}C. In a recent analysis [47] it has been pointed out that the conventional fixed core-plus-neutron model for halo nuclei is unable to explain the observed enhanced cross-section for these nuclei with any selection of neutron orbitals, and therefore a possibility of an enlarged core structure has been suggested. Experimental evidence of core modification in the near-drip nucleus ^{23}O has been recently reported in ref. [48].

The present RHB calculation reproduces the empirical one-neutron separation energies [41]. In particular, for ^{22}N we even obtain a slightly lower one-neutron separation energy, and the theoretical matter radius coincides with the one deduced from the experimental interaction cross-section. Also for ^{23}N, the calculated and empirical separation energies coincide, and the theoretical matter radius is only slightly below the large experimental error bar. The main difference is in the matter radii of the lighter isotopes (a similar situation also occurs for the fluorine isotopes, see fig. 6). The calculated radii are somewhat larger than the experimental values and therefore at $N = 15$ do not display the sharp discontinuity which, in ref. [8], is taken as evidence for the formation of the neutron halo. In the present calculation the gradual increase of matter radii reflects the formation of the neutron skin. This is shown in the upper right panel of fig. 4, where the values of $r_n - r_p$ are plotted as function of the neutron number, and in fig. 5 we display the self-consistent RHB neutron and proton ground-state density distributions of even-N nitrogen isotopes. It should be pointed out, however, that the formation of the halo structure can only be observed if calculations were performed in coordinate space. Moreover, particle number projection might be necessary in order to reproduce the sharp increase of matter radii. Finally, we note that the RHB NL3 + D1S calculation predicts the heaviest particle stable nitrogen isotope to be ^{23}N, in excellent agreement with recent data on the neutron drip line [10].

Very similar results are obtained for the fluorine isotopes. In fig. 6 we compare the RHB theoretical proton,

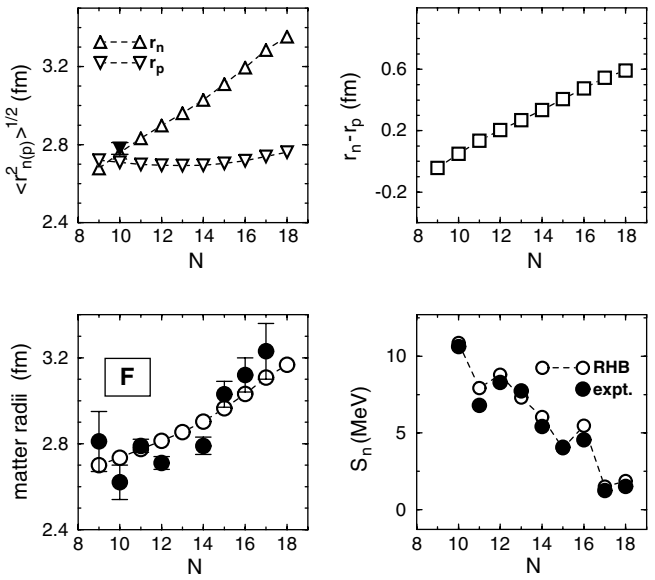

Fig. 6. The RHB theoretical proton, neutron and matter radii, skin thicknesses, and one-neutron separation energies of fluorine isotopes, compared with the experimental radii [44,2,8] and separation energies [41].

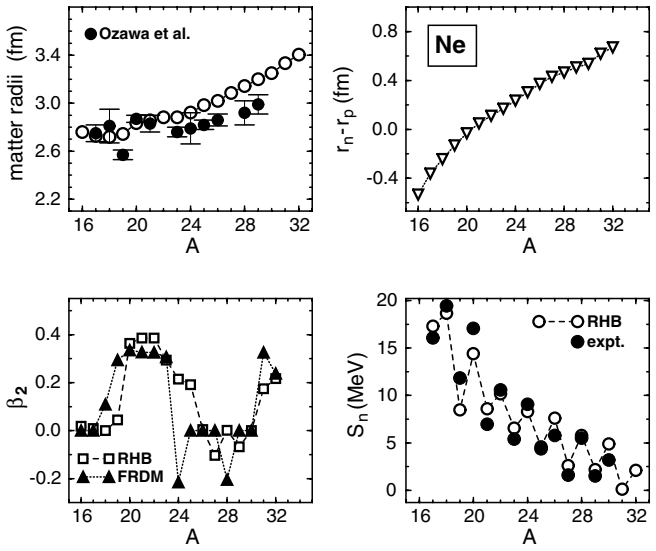

Fig. 7. Matter radii, diferences between neutron and proton radii, ground-state quadrupole deformations, and one-neutron separation energies of neon isotopes. The experimental values for the matter radii are from ref. [9] The calculated β_2 values are displayed in comparison with the predictions of the finite-range droplet model [40], and the separation energies are compared with experimental data [41].

neutron and matter radii, and one-neutron separation energies with the experimental radii [2,8,44] and separation energies [41]. The calculated matter radii do not reproduce the discontinuity at $N = 15$, though for the heaviest isotopes they are found within the experimental error bars. The calculated one-neutron separation energies reproduce the staggering between even-N and odd-N values. It is interesting to note that, like in the case of nitrogen, the RHB model with the NL3 + D1S effective interaction correctly predicts the location of the drip line [10]: the last bound isotope of fluorine is ^{31}F. Therefore, in agreement with experimental data, we obtain that the neutron drip line is at $N = 16$ for $Z = 7$, and at $N = 22$ for $Z = 9$. On the other hand, none of the standard RMF effective interactions reproduces the location of the drip line for oxygen. It has been argued that the sudden change in stability from oxygen to fluorine may indicate the onset of deformation for the neutron-rich fluorine isotopes [10]. In the present calculation, however, all fluorine isotopes up to ^{31}F turn out to be essentially spherical.

In ref. [17] we performed spherical RHB calculations of the Ne isotopic chain. In particular, we studied the formation of neutron halo structures in drip line Ne nuclei ($N > 20$). It was shown that the properties of the $1f$-$2p$ neutron orbitals near the Fermi level, and the neutron pairing interaction play a crucial role in the possible formation of the multi-neutron halo. In the present analysis we have performed calculations in the deformed harmonic-oscillator basis. In fig. 7 we display the matter radii, the $r_n - r_p$ values, the ground-state quadrupole deformations and the one-neutron separation energies of Ne isotopes. The matter radii are compared with the recently reported experimental values [9]. The agreement with experiment is very good. The calculated β_2 values are shown in comparison with the predictions of the finite-range droplet model [40], and the separation energies are compared with experimental data [41]. The FRDM and the present RHB calculation predict a similar mass dependence of the ground-state quadrupole deformation. We note two spherical regions around $A = 16$ and $A = 28$. Both models reproduce the large prolate deformations around $A = 20$, and predict prolate shapes in the region of possible halo structures $A \geq 30$. Pronounced differences in the predicted β_2 values are found for $A = 19$ and $A = 24$, 25. The latter probably indicates a region of shape coexistence. For $A = 28$ the FRDM predicts an oblate $\beta \approx -0.2$ deformation, while a spherical shape is calculated in the RHB model. The calculated separation energies reproduce the odd-even staggering and agree quite well with the experimental values.

The ground-state properties of the Na isotopic sequence are illustrated in fig. 8. The one-neutron separation energies are shown in comparison with experimental data [41]. The calculated values reproduce the empirical staggering between even- and odd-A isotopes, although for $A > 24$ the theoretical separation energies are systematically somewhat larger for the even-N isotopes. The calculated radii are compared with the experimental data: matter radii [5], neutron radii [3], and charge isotope shifts [49]. An excellent agreement between theory and experiment is obtained. For the matter and neutron radii the only significant difference is at $A = 22$, but this dip in the experimental sequence has recently been attributed to an admixture of the isomeric state in the beam [5]. Except for the lightest isotope shown, *i.e.* ^{20}Na, the calculated charge isotope shifts reproduce the

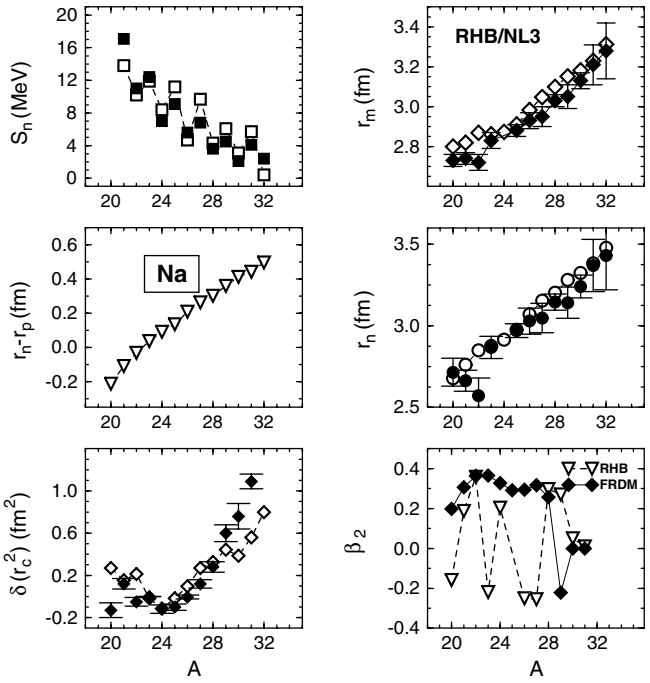

Fig. 8. One-neutron separation energies, radii, charge isotope shifts and ground-state quadrupole deformations of sodium isotopes. The RHB calculated values are compared with the experimental data: one-neutron separation energies [41], matter radii [5], neutron radii [3], charge isotope shifts [49], and with the β_2 values calculated in the finite-range droplet model [40].

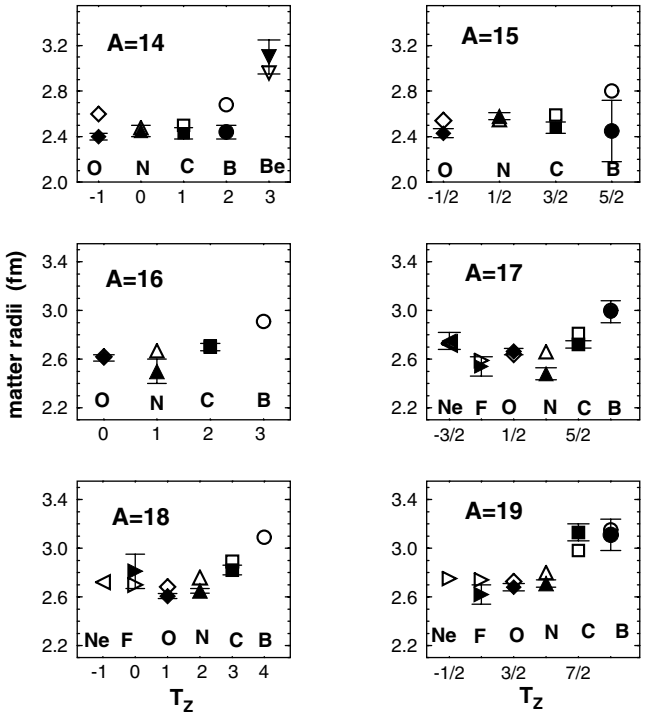

Fig. 9. The nuclear matter radii of the $A = 14, 15, 16, 17, 18, 19$ isobaric chains as functions of the isospin projection T_z. Results of fully self-consistent RHB calculations are compared with experimental data (for the description see the text).

Table 1. The calculated quadrupole moments Q (in barns) for several Na isotopes. The values in the parentheses correspond to the charge (proton) quadrupole moments Q_p.

A	Q (b)	(Q_p (b))	A	Q (b)	(Q_p (b))
20	−0.253	(−0.151)	26	−0.635	(−0.250)
21	0.324	(0.159)	27	−0.688	(−0.274)
22	0.689	(0.302)	28	0.764	(0.356)
23	−0.431	(−0.205)	29	0.689	(0.333)
24	0.450	(0.182)	30	0.154	(0.045)
25	−0.586	(−0.243)	31	0.041	(0.012)

empirical A-dependence. A significant difference between the theoretical and experimental values is observed only for $A \geq 29$. The calculated ground-state quadrupole deformations of the Na isotopes are compared with the predictions of the finite-range droplet model [40]. We note that, while the FRDM predicts all Na isotopes with $A \leq 28$ to be strongly prolate deformed, the result of the RHB calculation is the staggering between prolate and oblate shapes, indicating the onset of shape coexistence. In particular, ^{26,27}Na are predicted to be oblate, while prolate ground-state deformations are calculated for ^{28,29}Na. Very recent experimental data on quadrupole moments of $^{26-29}$Na [50] confirm this prediction. In table 1 we give the calculated intrinsic quadruple moments Q of the mass and charge distributions (Q and Q_p) for several Na isotopes.

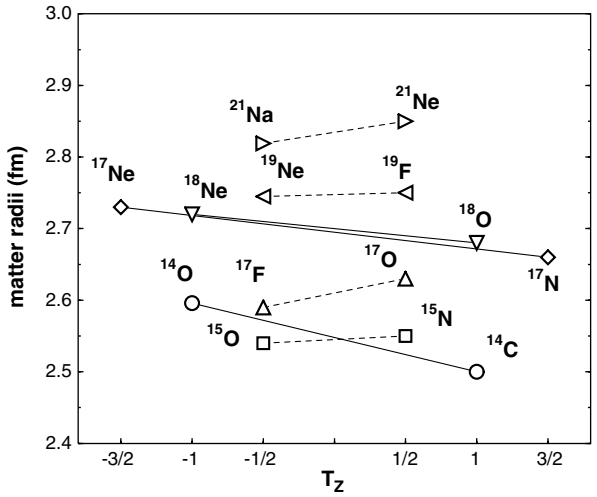

Fig. 10. Comparison of calculated matter radii for mirror nuclei as a function of the isospin projection T_z.

Our results for matter radii are summarized in fig. 9, where we plot the calculated values for the $A = 14, 15, 16, 17, 18, 19$ isobaric chains as functions of the isospin projection T_z. An excellent overall agreement is found between the experimental data and the matter radii calculated with the NL3 + D1S RHB effective interaction.

Finally, in fig. 10 the matter radii of mirror nuclei are compared as a function of the isospin projection T_z. It is interesting to note that for $\Delta T_z = 1$, the nuclei with

$T_z > 0$ have larger radii than their mirror partners with $T_z < 0$. Due to the strong effect of the Coulomb interaction, on the other hand, for $\Delta T_z = 2$ and 3 the proton-rich nuclei have almost 0.1 fm larger radii than their $T_z > 0$ mirror partners.

3 Summary

This work presents an analysis of ground-state properties of Be, B, C, N, F, Ne and Na isotopes in the framework of the Relativistic Hartree-Bogoliubov (RHB) model. In the last couple of years this model has been very successfully applied in the description of nuclear-structure phenomena in medium-heavy and heavy exotic nuclei far from the valley of β-stability and of the physics of the drip lines. The present analysis covers a region which is probably at the low-mass limit of applicability of the mean-field framework. This work is also a continuation of our previous applications of the RHB model of ref. [18] (spherical RHB calculations of neutron-rich isotopes of N, O, F, Ne, Na and Mg), and of ref. [29] (deformed RHB calculations of ground-state properties of the $A = 20$ isobaric sequence).

The present calculation has been performed in the configuration space of deformed harmonic-oscillator basis states. The NL3 effective interaction has been used for the mean-field Lagrangian, and pairing correlations have been described by the pairing part of the finite range Gogny interaction D1S. The calculated neutron separation energies, quadrupole deformations, nuclear matter radii, and differences in radii of proton and neutron distributions have been compared with very recent experimental data. For the neutron drip line nucleus ^{14}Be the RHB calculation predicts a large prolate deformation $\beta_2 = 0.36$ and the ratio of neutron to proton quadrupole moments $Q_n/Q_p = 3.6$. For the neutron-rich boron isotopes, the calculated matter radii reproduce the recent experimental data [6] for ^{17}B and ^{19}B. This is an important result, since ^{19}B ($T_z = 9/2$) has one of the largest N/Z values known at present in the low-mass region of the nuclear chart.

Even though the present calculation, performed in the deformed harmonic-oscillator configuration space, cannot reproduce the anomalous matter radius of the one-neutron halo nucleus ^{19}C, the neutron separation energy 510 keV is in excellent agreement with the experimental value 530 ± 130 keV obtained from an analysis of the angular distribution of the $^{18}\mathrm{C} + n$ center of mass [46]. A large oblate deformation $\beta_2 \approx -0.4$ is predicted for ^{19}C.

The RHB model with the NL3 + D1S effective interaction predicts the location of the neutron drip line in nitrogen and fluorine in agreement with recent experimental findings [10]: the heaviest particle stable isotopes are ^{23}N and ^{31}F. The calculation, however, does not reproduce the location of the neutron drip line in oxygen. The calculated matter radii of the neutron-rich nitrogen and fluorine isotopes are in agreement with very recent experimental data [8]. The sudden increase of the radii at $N = 15$, which was taken as evidence for the formation of the neutron halo, is not reproduced by the present calculation.

For the neutron-rich neon isotopes the RHB model predicts pronounced prolate deformations in the region of possible halo structures ($A > 30$). The calculated matter radii are in very good agreement with recent experimental data [9]. For the Na isotopic sequence the calculated radii are in excellent agreement with experimental data on matter radii [5], neutron radii [3], and charge isotope shifts [49]. The calculated ground-state quadrupole deformations are confirmed by the recent experimental data on quadrupole moments of $^{26-29}$Na [50].

This work has been supported in part by the Bundesministerium für Bildung und Forschung under project 06 MT 193, by the Deutsche Forschungsgemeinschaft, and by the Gesellschaft für Schwerionenforschung (GSI) Darmstadt.

References

1. I. Tanihata *et al.*, Phys. Lett. B **206**, 592 (1988).
2. A. Ozawa *et al.*, Phys. Lett. B **334**, 18 (1994).
3. T. Suzuki *et al.*, Phys. Rev. Lett. **75**, 3241 (1995).
4. A. Ozawa *et al.*, Nucl. Phys. A **608**, 63 (1996).
5. T. Suzuki *et al.*, Nucl. Phys. A **630**, 661 (1998).
6. T. Suzuki *et al.*, Nucl. Phys. A **658**, 313 (1999).
7. T. Suzuki *et al.*, Phys. Rev. Lett. **89**, 012501 (2002).
8. A. Ozawa *et al.*, Nucl. Phys. A **691**, 599 (2001).
9. A. Ozawa *et al.*, Nucl. Phys. A **693**, 32 (2001).
10. H. Sakurai *et al.*, Phys. Lett. B **448**, 180 (1999).
11. P.J. Woods, C.N. Davids, Annu. Rev. Nucl. Part. Sci. **47**, 541 (1997).
12. Y.N. Novikov *et al.*, Nucl. Phys. A **697**, 92 (2002).
13. A. Leistenschneider *et al.*, Phys. Rev. Lett. **86**, 5442 (2001).
14. L. Chulkov, Nucl. Phys. A **603**, 219 (1996).
15. J. Gómez del Campo *et al.*, Phys. Rev. Lett. **86**, 43 (2001).
16. J. Meng, P. Ring, Phys. Rev. Lett. **77**, 3963 (1996).
17. W. Pöschl, D. Vretenar, G.A. Lalazissis, P. Ring, Phys. Rev. Lett. **79**, 3841 (1997).
18. G.A. Lalazissis, D. Vretenar, W. Pöschl, P. Ring, Nucl. Phys. A **632**, 363 (1998).
19. G.A. Lalazissis, D. Vretenar, W. Pöschl, P. Ring, Phys. Lett. B **418**, 7 (1998).
20. G.A. Lalazissis, D. Vretenar, P. Ring, M. Stoitsov, L. Robledo, Phys. Rev. C **60**, 014310 (1999).
21. J. Meng, P. Ring, Phys. Rev. Lett. **80**, 460 (1998).
22. J. Meng, Nucl. Phys. A **654**, 702c (1999).
23. G.A. Lalazissis, D. Vretenar, P. Ring, Phys. Rev. C **57**, 2294 (1998).
24. J. Meng, Nucl. Phys. A **635**, 3 (1998).
25. J. Meng, I. Tanihata, Nucl. Phys. A **650**, 176 (1999).
26. D. Vretenar, G.A. Lalazissis, P. Ring, Phys. Rev. Lett. **82**, 4595 (1999).
27. G.A. Lalazissis, D. Vretenar, P. Ring, Nucl. Phys. A **650**, 133 (1999).
28. G.A. Lalazissis, D. Vretenar, P. Ring, Nucl. Phys. A **679**, 481 (2001).
29. G.A. Lalazissis, D. Vretenar, P. Ring, Phys. Rev. C **63**, 034305 (2001).
30. P. Ring, Prog. Part. Nucl. Phys. **37**, 193 (1996).
31. J. Boguta, A.R. Bodmer, Nucl. Phys. A **292**, 413 (1977).

32. W. Pöschl, D. Vretenar, P. Ring, Comput. Phys. Commun. **103**, 217 (1997).
33. Y.K. Gambhir, P. Ring, A. Thimet, Ann. Phys. (N.Y.) **198**, 132 (1990).
34. M. Serra, P. Ring, Phys. Rev. C **65**, 064324 (2002).
35. G.A. Lalazissis, J. König, P. Ring, Phys. Rev. C **55**, 540 (1997).
36. J.F. Berger, M. Girod, D. Gogny, Nucl. Phys. A **428**, 32 (1984).
37. P.-G. Reinhard, M. Rufa, J. Maruhn, W. Greiner, J. Friedrich, Z. Phys. A **323**, 13 (1986).
38. M.M. Sharma, M.A. Nagarajan, P. Ring, Phys. Lett. B **312**, 377 (1993).
39. Y. Sugahara, H. Toki, Nucl. Phys. A **579**, 557 (1994).
40. P. Möller, J.R. Nix, W.D. Myers, W.J. Swiatecki, At. Data Nucl. Data Tables **59**, 185 (1995).
41. G. Audi, A.H. Wapstra, Nucl. Phys. A **595**, 409 (1995).
42. M. Fukada *et al.*, Phys. Lett. B **268**, 339 (1991).
43. J.H. Kelley *et al.*, Phys. Rev. Lett. **74**, 30 (1995).
44. H. de Vries, C.W. de Jager, C. de Vries, At. Data Nucl. Data Tables **36**, 495 (1987).
45. D. Bazin *et al.*, Phys. Rev. Lett. **74**, 3569 (1995).
46. T. Nakamura *et al.*, Phys. Rev. Lett. **83**, 1112 (1999).
47. R. Kanungo, I. Tanihata, A. Ozawa, Phys. Lett. B **512**, 261 (2001).
48. R. Kanungo *et al.*, Phys. Rev. Lett. **88**, 142502 (2002).
49. E.W. Otten, in *Radii Isotope Shifts by Laser Beam Spectroscopy*, edited by D.A. Bromley, Vol. **8** (Plenum, New York, 1989) p. 515.
50. M. Keim *et al.*, Eur. Phys. J. **8**, 31 (2000).